Valorization of Poplar Wood Wastes Into 3D-Printed Soya Oil-Based Composites by Vat Photopolymerization for Interior Design

Journal of Polymer Science

WILEY

JOURNAL OF POLYMER SCIENCE

RESEARCH ARTICLE OPEN ACCESS

Valorization of Poplar Wood Wastes Into 3D-Printed Soya Oil-Based Composites by Vat Photopolymerization for Interior Design

Francesca Sacchi[1] | Tiziano Uriel Monteu Cotto[2] | Giovanna Colucci[1,3] | Guido Callegari[2] | Paolo Simeone[2] | Daniela Bosia[2] | Federica Bondioli[1,3] | Massimo Messori[1,3]

[1]Department of Applied Science and Technology (DISAT), Politecnico di Torino, Turin, Italy | [2]Department of Architecture and Design (DAD), Politecnico di Torino, Turin, Italy | [3]National Interuniversity Consortium of Materials Science and Technology (INSTM), Florence, Italy

Correspondence: Giovanna Colucci (giovanna.colucci@polito.it)

Received: 27 December 2025 | **Revised:** 20 March 2026 | **Accepted:** 26 March 2026

Keywords: acrylate epoxidized soybean oil (AESO) | additive manufacturing (AM) | liquid crystal display (LCD) | poplar wood | vat photopolymerization

ABSTRACT

The research aims to develop innovative bio-based polymer composites through vat photopolymerization (VPP) 3D printing (3DP) and to test their use in creating a joint for furniture design, thereby constituting a proof of concept for the project "Made in Italy Circolare e Sostenibile-MICS." Formulation composed of 50 wt% acrylate epoxidized soybean oil (AESO) resin and 50 wt% isobornyl methacrylate (IBOMA) as a reactive diluent is prepared with 2 phr phenylbis(2,4,6-trimethylbenzoyl) phosphine oxide (BAPO) as a radical photoinitiator. The photopolymerization is conducted using liquid crystal display (LCD) 3DP technology. Two different poplar wood powders (namely, P_I and P_{IV}), obtained from waste materials of the plywood manufacturing process, are incorporated into the resin at concentrations of 3 phr to produce the final bio-based composites. Sedimentation and rheological tests are carried out on the photocurable resins to assess their viscosity and 3D printability. Once the optimal printing parameters are established, specimens for mechanical characterization and different structures, gradually evolving into more intricate designs, are 3D-printed. The results show that the bio-composites represent a promising alternative for producing joints, connections, nuts, and screws for various design applications, exhibiting high dimensional accuracy, high resolution, and well-defined geometries.

1 | Introduction

Polymeric materials have become increasingly important due to their remarkable performance and cost-effectiveness. Their wide-ranging characteristics make them essential in various fields, attracting strong attention from scientists in both academia and industry. Moreover, polymers are crucial in additive manufacturing (AM), enabling the creation of tailor-made components suitable for specific applications, such as automotive, building, coatings, microelectronics, and medical industries [1, 2]. AM includes various technologies that build physical items by depositing material layer upon layer, modeled by computer-aided design (CAD) software. This digital model is then converted and saved in the standard tessellation language (STL) file format. Specialized software processes the STL file by dividing the model into a sequence of parallel 2D layers, defining each layer's shape for the printing process [2]. At present, AM technologies based on polymeric materials are used in various application fields, including engineering, medicine, education, architecture, cartography, toys, and entertainment [3]. The ISO/ASTM 52900:2015(E) standard defines AM as "a process of joining materials to create parts

Francesca Sacchi and Tiziano Uriel Monteu Cotto contributed equally to this work.

from 3D model data, typically layer by layer, in contrast to subtractive manufacturing techniques."

This definition emphasizes the key difference between AM, which builds objects layer by layer from a digital model [4, 5]. AM technologies offer numerous advantages over traditional manufacturing methods, like greater design flexibility, reduced material waste, shorter production times, and the ability to create complex geometries that would be difficult or impossible to achieve using conventional technologies [6–8].

Among the various AM technologies for polymer processing, vat photopolymerization (VPP) stands out for its capability to fabricate 3D printed objects with intricate and hierarchical geometries, utilizing thermosetting photocurable resins. This technology cures the liquid resin layer by layer into solid structures through a photopolymerization reaction triggered by UV radiation, working in two different configurations: bottom–up and top–down [9, 10].

Liquid crystal display (LCD) represents a recent innovation in VPP technology where light is emitted directly through an LCD screen onto the uncured resin, preventing light from scattering and minimizing pixel distortion compared to the conventional digital light processing (DLP) printing [11, 12]. The process offers several advantages, including the ability to work with a wide range of thermoset polymers and the flexibility to experiment with various polymeric resins and composites. This allows for customization of photopolymers by altering their material properties or even developing entirely new types of materials.

The resolution of the printing process depends on several factors, as the resolution of the LCD screen itself (in pixels) is one key factor; the physical size of the screen also plays a role, larger screens will have larger pixels, which results in lower spatial resolution.

Therefore, the XY resolution, which refers to the size of a single pixel projected onto the printing plane, is a crucial factor. Whereas the Z resolution, or the thickness of each printed layer, is determined by the vertical movement precision of the build platform [13]. The process efficiently uses inexpensive raw materials and supports high-resolution output, aligning well with other sustainable alternatives. However, the lack of eco-friendly photopolymerizable resins limits their use in large-scale applications [6, 14].

Furthermore, unlike thermal polymerization, which usually requires high temperatures, photopolymerization can occur at room temperature. This eliminates the need for heat and often reduces or completely avoids the release of volatile organic compounds (VOCs).

To facilitate the transition to a circular economy, in addition to the use of greener and more eco-friendly technologies, like AM, the development of innovative bio-based resins for 3DP could play a crucial role [6]. In this context, vegetable oils (VOs) are among the most used materials due to their abundance, renewability, low cost, biodegradability, and desirable structural features, which make them highly attractive for a wide variety of applications.

VOs contain unsaturated fatty chains that can be chemically modified to produce epoxidized and acrylated derivatives, which are photopolymerizable under UV–Vis radiation. After chemical modification reactions, like epoxidation and acrylation, they become photopolymerizable by using UV–Vis radiation [15]. They are a viable and sustainable alternative to traditional petrochemical-based resins. Although the literature provides a wealth of studies on 3D printed polymer composites, the use of bio-based monomers and fillers derived from industrial wastes, such as soybean oil resin, for creating composites via LCD has been underexplored compared to other technologies, like DLP [16–18]. Moreover, bio-fillers can be incorporated into VOs to enhance mechanical properties and expand the range of applications for 3D printed components [13, 18–29]. Among the different bio-fillers used, poplar wood powders derived from plywood manufacturing wastes can represent a valid alternative [30].

Poplars include species such as trembling aspen, bigtooth aspen, balsam poplar, eastern cottonwood, and black cottonwood. They are fast-growing, moisture-loving, shade-intolerant trees with relatively short lifespans. The wood is lightweight, with a diffuse-porous structure and moderate strength, exhibiting bending and stiffness properties like those of spruce, pine, and fir. It is composed mainly of fibers (53%–60%), vessel elements (28%–34%), and ray cells (11%–14%), with minimal axial parenchyma.

Chemically, poplar wood is rich in polysaccharides (almost 80% holocellulose: 40%–50% cellulose, 15%–30% hemicellulose) and has low lignin content (20%–30%). It is widely used in pulp and paper, lumber, plywood, composites, furniture, packaging, and various utility products, with composites capitalizing on the combined strengths of constituent materials [31, 32]. The principal wood-based product manufactured from polar wood is plywood [33]. Plywood is a lightweight, versatile building material made by bonding at least three thin wood veneers (1–5 mm thick) with adhesive, each layer oriented orthogonally. Commonly used in furniture, it is valued for its strength and adaptability [34].

This research work uses poplar wood powder waste from the plywood industry due to two main reasons: its widespread use in furniture and construction, and the prominence of poplar cultivation in Italy's agro-industrial sector [33]. In 2019, Italy dedicated approximately 58,000 ha to poplar cultivation, yielding around 1 million cubic meters of roundwood annually, mainly in the northern regions [35]. The paper aims to establish a framework for reusing fibrous waste from traditional Italian agro-industrial supply chains, promoting the development of innovative materials and products with minimal environmental impact. In plywood production, poplar logs are first transported to the facility, debarked, and peeled into thin veneer sheets. These sheets are dried and undergo an initial quality check, with substandard sheets discarded. The remaining sheets are stacked orthogonally and glued, then pressed into a single panel. A squaring and sanding process follows, refining dimensions and surface quality. After a final quality inspection, panels are

stored or packaged for distribution [33]. The process described is schematically illustrated as a flowchart in Figure 1.

The main by-product of plywood panel production is roundwood, a cylindrical wooden residue approximately 10 cm in diameter and 2 m in length, left after the peeling stage, used to produce veneers. This residue is typically downcycled as biomass for energy recovery, but it can also undergo thermotreatment for reuse in pallet and packaging production [36].

In the final stages of panel manufacturing, squaring and sanding processes are performed to regularize the geometry and thickness of the panels. These operations generate dust and small wood flakes, which are commonly used as biomass. Depending on the extraction and storage method, these residues may appear in loose form or as briquettes.

The goal of this research is to develop innovative bio-based polymer composites by incorporating poplar wood waste powders into a bio-based photocurable resin for design applications. Using LCD-based VPP, a series of components were successfully printed in 3D, including objects with considerable potential applications in interior design, such as joints and connections, screws, bolts and nuts, plates and covers, highlighting the suitability of producing customized, sustainable elements for interior and design-oriented applications.

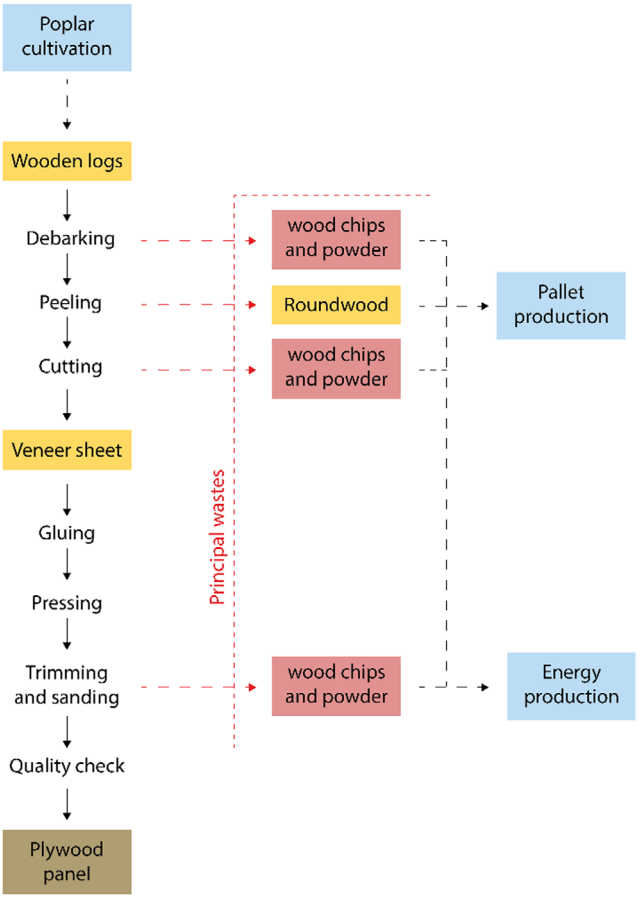

FIGURE 1 | Flowchart of the main stages of plywood production, with waste in red, by-products in yellow, and processes that reuse it most highlighted in blue.

The resulting photocurable formulations and composites were thoroughly characterized in terms of their thermal, morphological, rheological, viscoelastic, and mechanical properties. This work also aims to combine the advantages of bio-based composites, produced by valorizing bio-fillers derived from industrial waste of plywood production, one of the industrial processes that represents one of the most widespread and efficient forms of wood used globally, with the potential of AM technologies.

2 | Materials Characterizations

2.1 | Characterization of the Poplar Powders

Thermogravimetric (TGA) analysis was conducted with a Mettler-Toledo TGA 851e instrument (Columbus, OH, USA). Samples of approximately 10 mg were heated from 25°C to 900°C at a rate of 10°C min^{-1} in air (50 mL min^{-1}). TGA curves were normalized to each powder mass, and derivative thermogravimetric (DTG) curves were generated from their respective thermograms.

Morphology and energy-dispersive x-ray spectroscopy (EDS) of the powders were examined using a Phenom XL Scanning Electron Microscope (Thermo Fisher Scientific, Waltham, MA, USA) operating at 15 kV. Before analysis, samples were coated with platinum for 20 s using a Quorum Sputter Coater Q150T S (Laughton, East Sussex, UK).

The shape properties of poplar powders, including diameter, aspect ratio, circularity, and size, were analyzed using the Morphology 4 automated system (Malvern Panalytical, UK). A 3 mm^3 volume of dry powder was spread onto a glass plate for testing, with dispersion conducted under a high pressure of 4 bar and an injection time of 10 ms.

The powder density was determined using a helium pycnometer (Ultrapyc 5000, Anton Paar GmbH, Graz, Austria) at a temperature of 20°C. Measurements were conducted using a small cell volume, and the analysis was performed in pulse preparation mode and repeated for 15 cycles. The results allowed the volume fraction (Φ) of the powders in the liquid formulation, by following Equation (1):

$$\Phi = \frac{\left(\frac{m_f}{\rho_f}\right)}{\left[\frac{m_f * \rho_f}{m_m * \rho_m}\right]} \quad (1)$$

where m_f is the mass of filler, ρ_f is the density of filler, m_m is the mass of monomer, ρ_m is the density of AESO.

2.2 | Characterization of the Photocurable Formulations

The viscosity of the formulations was measured at 25°C using an Anton Paar MCR 702e MultiDrive rheometer (Graz, Austria), equipped with a 25 mm parallel plate setup and a gap of 0.200 mm. For each formulation, three independent measurements were performed over a shear rate range from 0.01 to 100 s^{-1}, yielding consistent results across replicates and confirming the reliability of the data.

The photo-curing process was analyzed using photo-DSC (p-DSC) with a Mettler-Toledo DSC-1 system equipped with a GC100 Gas Controller. The DSC features an optical fiber connected to a mercury lamp source (Hamamatsu LIGHTINGCURE LC8 from Hamamatsu Photonics) emitting a broad spectrum of light. A filter centered the UV emission at 365 nm, with an intensity of approximately 100 mW cm^{-2}. Around 8 mg of the formulation was placed in an open 40 μL aluminum pan, while an empty pan served as the reference. Experiments were conducted at 25°C under a controlled nitrogen atmosphere (flow rate of 40 mL min^{-1}). The samples underwent two 10-min irradiation cycles to thoroughly assess the UV-curing behavior. The second irradiation run verified the completion of curing and established the baseline.

2.3 | Characterization of the Photocured 3D Samples

The insoluble fraction, or gel content, was evaluated by measuring the weight loss after 24 h of chloroform extraction at 25°C, following the ASTM D2765-84 standard.

TGA analysis was conducted with a Mettler-Toledo TGA 851e instrument (Columbus, OH, USA) in the same conditions used for the poplar powders testing around 10 mg of composite sample.

The specimen morphology was examined using a Phenom XL Scanning Electron Microscope (Thermo Fisher Scientific, Waltham, MA, USA) operating at 15 kV. Before analysis, samples were coated with platinum for 20 s using a Quorum Sputter Coater Q150T S (Laughton, East Sussex, UK). Each specimen was fractured in liquid nitrogen, and the fracture surfaces were analyzed.

Dynamic mechanical thermal analysis (DMTA) was performed over a temperature range of −5°C to 140°C using an Anton Paar MCR 702e Multi Drive Rheometer (Graz, Austria) at a frequency of 1 Hz in tensile mode. The tested samples were rectangular, measuring 35 mm in length, 10 mm in width, and 2 mm in thickness. By assessing the storage modulus at temperatures well above the polymer glass transition temperature (T_g), where T_g is obtained from DMTA analysis by analyzing the maximum peak of TanDelta curves as a function of temperature. Moreover, the volumetric crosslinking density of the cross-linked network (ν_e) of the polymer network was calculated using the classical rubber elasticity theory, as described in Equation (2):

$$\nu_e = \left(\frac{E'}{3RT}\right) \tag{2}$$

where T is the absolute temperature (in Kelvin), E' is the storage modulus in the rubbery plateau ($T_g + 50$°C), and R represents the universal gas constant [37, 38].

Mechanical properties were assessed via tensile tests following the ISO 527-2 standard. The tests were carried out using an Instron 5966 machine equipped with a 2 kN load cell and pneumatic grips. A deformation rate of 2 mm min^{-1} and a grip separation of 50 mm were employed. Deformation was determined using a displacement transducer. The specimens 5A had dog bone shapes with gauge lengths of 26 mm, widths of 4 mm, and thicknesses of 2 mm.

3 | Results and Discussion

3.1 | Poplar Powder Characterizations

To achieve a more comprehensive understanding of the role of the filler addition in the developed 3D-printed composites and their final properties, the two poplar powders were thoroughly characterized from thermal and morphological points of view.

Figure 2 reports TG (a) and the derivative DTG (b) curves performed on P_I and P_{IV} powders, respectively.

Figure 2a shows the percentage mass variation as a function of temperature of the two poplar wood powders. Both show a significant mass loss between 200°C and 450°C, the range in which the thermal degradation of the main biomass components occurs, such as hemicellulose, cellulose, and lignin [32]. P_I starts to lose mass at slightly lower temperatures with respect to P_{IV}. Above 400°C, the residual mass tends to stabilize, indicating that most of the filler degradation is complete.

Figure 2b, relating to DTG curves, shows the mass loss rate versus temperature. Both powders exhibit very similar profiles, characterized by three distinct peaks: one at around 290°C, associated with the hemicellulose degradation; a second peak at around 310°C–320°C related to cellulose decomposition; and a third degradation peak at temperature above 400°C, attributable to lignin fraction [31, 32], the last component to degrade, due to its aromatic structure [39, 40].

Furthermore, both poplar powders show an ash content of 5 and 6 wt% for P_I and P_{IV}, respectively, resulting from the inorganic elements present in the poplar wood powders, like phosphorus (P), potassium (K), calcium (Ca), and magnesium (Mg), which are their macronutrients and give information about the main nutrients present in the soil [32]. The presence of these inorganic elements was confirmed by EDS analysis, revealing an average percentage by mass in the powders equal to: Ca 2.19% ± 0.17%, K 0.52% ± 0.11%, P 0.14% ± 0.05% and Mg 0.12% ± 0.04%. P_{IV} shows slightly higher ash content, probably due to the different starting feedstock. All the thermal data obtained for the two poplar powders are summarized in Table 1.

SEM images were also acquired to examine the morphology of the P_I (a–b) and P_{IV} (c–d), as reported in Figure 3. The morphology of P_I presents an irregular and fragmented structure. At higher magnifications, P_I shows fractured and broken fragments with irregular surfaces, as visible from Figure 3a,b. The lack of structural cohesion is evident, with a disordered and poorly integrated arrangement. On the contrary, the P_{IV} structure appears denser and more compact from the first magnification, with particles with a lamellar morphology and a more regular structure. P_{IV} maintains the lamellar microstructure

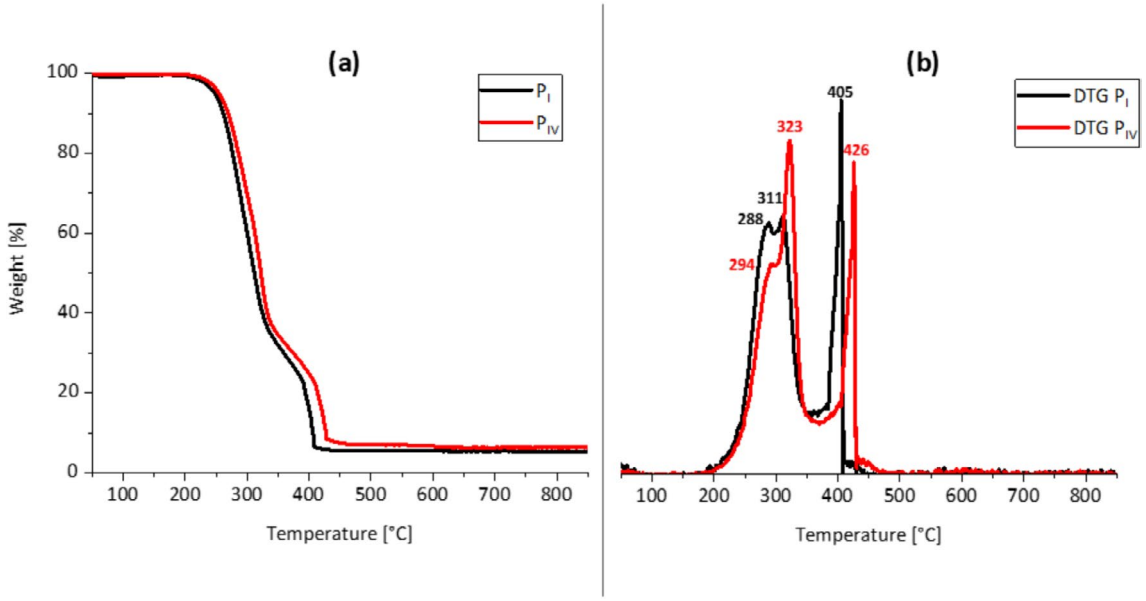

FIGURE 2 | TGA (a) and DTG curves (b) of the two poplar wood powders.

TABLE 1 | Main thermal properties of the two poplar wood powders.

Sample code	$T_{5\%}$ [a] (°C)	$T_{maxdegr}$ [b] (°C)	Ash content [c] (%)
P_I	249	288–311–405	5
P_{IV}	256	294–323–426	6

[a] $T_{5\%}$ represents the temperature at which 5% of the mass is lost.
[b] $T_{maxdegr}$ is the temperature at which the degradation rate is maximum.
[c] Ash content was evaluated at 900°C.

at higher magnifications, as shown in Figure 3c,d, with particles that fold and overlap like thin sheets. The surfaces appear more uniform. For both powders, the particles tend to aggregate in compact structures, as results obtained from PSD characterization.

To better investigate the particle size distribution of poplar powders, a granulometric analysis was performed by examining many poplar powder particles. The values of the particle size distribution, aspect ratio, and circularity of the two poplar powders evaluated by morphological imaging are listed in Table 2.

The results indicate that P_I particles have an average diameter of 2 μm, an average aspect ratio of 0.7, and an average circularity close to 0.80. P_{IV} particles, on the other hand, show an average diameter of 6 μm, an average aspect ratio of 0.7, and an average circularity close to 0.8. Therefore, P_{IV} particles are larger and more heterogeneous, characterized by greater variability in size, some of which are very large and likely clusters. The aspect ratio indicates how elongated the particles are; a value of 1 means a perfect circle; values lower than 1 indicate more elongated particles. From the results obtained, both powders have moderately elongated particles, with P_I slightly rounder in the median but more variable. Regarding circularity, values close to 1 indicate rounder particles. Circularity is very similar between the two powders. Both have good average roundness, but P_I shows greater variability, with some particles less circular. SEM analysis had already highlighted these differences, which were quantified by morphological analysis.

3.2 | Photocurable Formulations Characterization

The viscosity results of the photocurable formulations are shown in Figure 4 and summarized in Table 3. All formulations exhibit a decrease in viscosity as the shear rate increases. At higher shear rates, the formulations display a plateau region where viscosity becomes nearly constant. The viscosity of the unfilled formulation increases with the addition of poplar wood powders, but the viscosity remains below the instrumental viscosity required for VPP [41, 42].

The shear rate was selected at 100 s^{-1} because it is a value commonly used to represent processing conditions relevant to VPP technologies, where the resin experiences moderate shear during recoating and flow. Therefore, this value was chosen to provide a representative and comparable assessment of the viscosity of the different formulations. Continuous lines represent the corresponding Carreau model, which provides a fit to the data, enabling interpolation across the measured shear rate range and a clear visualization of the overall rheological behavior. Comparison between the experimental data and the Carreau fits shows excellent agreement across all shear rates, with $R^2 \geq 0.9986$ for all systems. At high shear rates, the fit reproduces almost exactly the measured viscosities. For example, at 100 s^{-1}, the experimental viscosities are 170, 185, and 272 mPa s for A-IB, A-IB + 3P_I, and A-IB + 3P_{IV}, respectively, while the corresponding Carreau fit values are 175, 194, and 288 mPa s, demonstrating that the model converges with the experimental data.

Overall, the Carreau fits allow interpolation between the discrete experimental measurements, providing a quantitative description of the shear-thinning behavior and enabling direct comparison of the rheological properties of the formulations. Figure 4

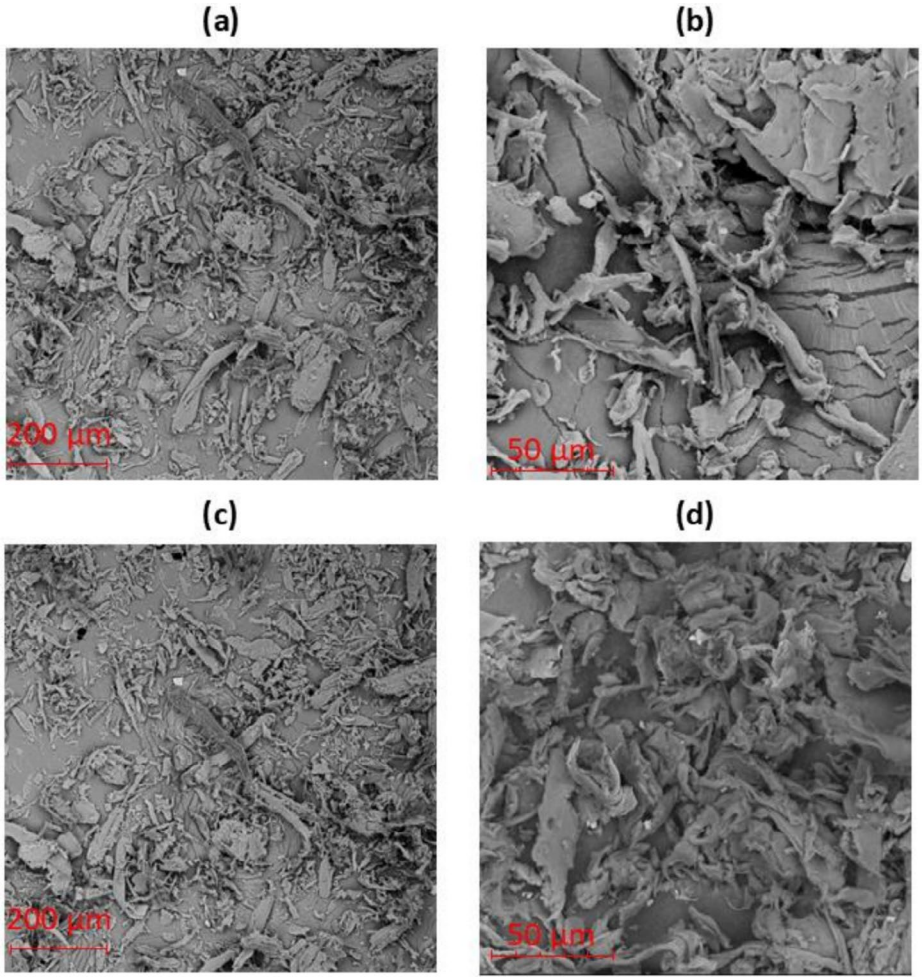

FIGURE 3 | SEM micrographs at different magnifications, 300× and 1500×, of P_I (a, b) and P_{IV} (c, d).

TABLE 2 | Poplar powders diameter, aspect ratio, and circularity evaluated by PSD analysis.

Sample code	Diameter (µm)	Aspect ratio	Circularity
P_I	D [n, 0.1]: 0.3	D [n, 0.1]: 0.4	D [n, 0.1]: 0.5
	D [n, 0.5]: 0.9	D [n, 0.5]: 0.8	D [n, 0.5]: 0.9
	D [n, 0.9]: 3.8	D [n, 0.9]: 0.9	D [n, 0.9]: 0.9
P_{IV}	D [n, 0.1]: 1.5	D [n, 0.1]: 0.4	D [n, 0.1]: 0.6
	D [n, 0.5]: 2.2	D [n, 0.5]: 0.7	D [n, 0.5]: 0.9
	D [n, 0.9]: 14.8	D [n, 0.9]: 0.9	D [n, 0.9]: 0.9

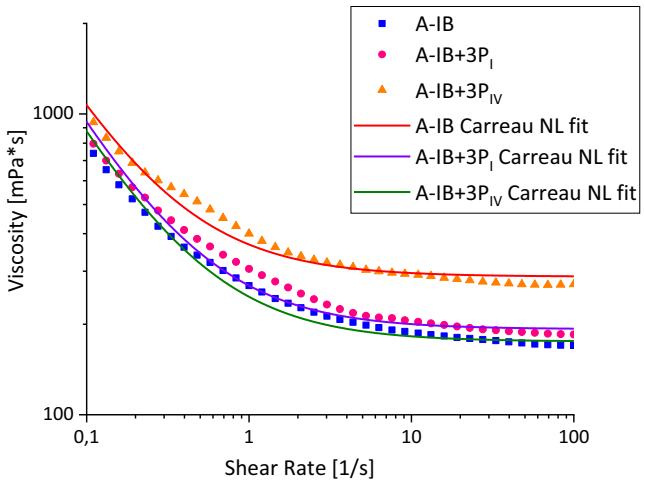

FIGURE 4 | Viscosity as a function of shear rate for the three systems: A-IB, A-IB + $3P_I$, and A-IB + $3P_{IV}$. Experimental data are shown as discrete points, while continuous lines represent the corresponding Carreau model fits.

clearly presents both the individual experimental data points and the fitted curves, accurately representing the influence of poplar powder addition on the viscosity across the entire shear rate range. The Carreau model was selected because it accurately describes the shear-thinning behavior of non-Newtonian fluids, as expressed in Equation (3). This allows a realistic estimation of the viscosity and facilitates direct comparison of the effects of powder addition on the rheological properties of the systems [43]. The excellent agreement with the experimental

data, indicated by $R^2 \geq 0.9986$, further supports the suitability of this model for representing the flow behavior of all three studied formulations.

$$\mu = \mu_\infty + \frac{\mu_0 - \mu_\infty}{\left[1 + (\lambda \bar{\gamma})^a\right]^{\frac{1-n}{a}}} \quad (3)$$

where μ_0 is the viscosity at zero shear rate; μ_∞ is the infinite shear rate viscosity; λ is the time constant; $\bar{\gamma}$ is the shear rate; a is the parameter that defines the shape of the transition; n is the flow index. If $n < 1$, as happens in these studied systems, it means that they are pseudoplastic fluids, which exhibit shear-thinning behavior, that is, the viscosity decreases as the shear rate increases. This means that at low shear rates, the viscosity remains extremely high, corresponding to the zero-shear viscosity μ_0, while even a small increase in shear rate leads to a rapid decrease of the viscosity toward the high-shear plateau μ_∞, as clearly visible in Figure 4. The results, summarized in Table 3, indicate that the nature of the fillers can affect the system's viscosity differently depending on the type of poplar wood powder, presumably due to variations in their origin, chemical composition, and surface morphology.

Notably, the densities of the two poplar powders, measured with the pycnometer, are 1.516 g cm^{-3} for P_I and 1.517 g cm^{-3} for P_{IV}, indicating that the volume fraction of the two powders in the mixtures is approximately the same (2.01% as calculated using Equation 1) and thus is irrelevant to the different viscosity [31, 32]. Photo-DSC analysis allowed for assessment of the influence of poplar powders on the reactivity of the system, as shown in Figure 5.

TABLE 3 | Viscosity of photocurable formulations evaluated at 25°C and 100 s^{-1} shear rate.

Sample code	Viscosity (mPa s)
A-IB	170
A-IB + 3P_I	185
A-IB + 3P_{IV}	266

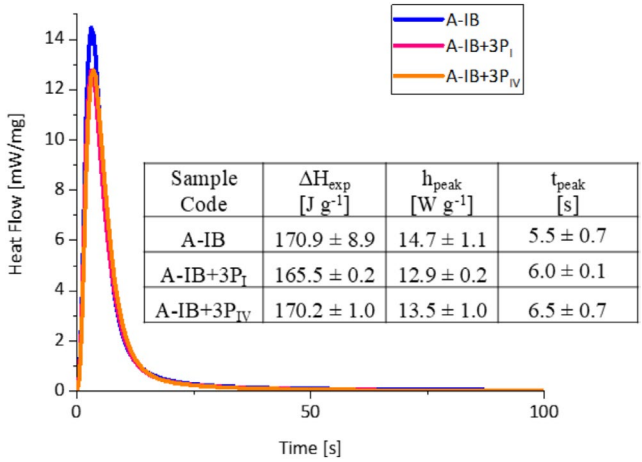

FIGURE 5 | Comparison among p-DSC curves of AESO-based photocurable formulations.

ΔH_{exp}, which indirectly reflects the overall conversion degree [37] obtained by performing the integral of each curve, is very similar among the samples, with a slight decrease observed in the A-IB + 3P_I sample. h_{peak}, which corresponds to the maximum heat flux recorded during the thermal event [37], shows a reduction from A-IB to filled samples. t_{peak} represents the time at which the exothermic reaction reaches its peak [37] and is around 5.5 s for A-IB and tends to slightly increase in the samples containing poplar powders.

In summary, the addition of 3 phr of P_I and P_{IV} seems to primarily influence the kinetics and intensity of the thermal events, resulting in a slight delay in peak time and a reduction in peak power, while leaving the transition enthalpy largely unchanged. Therefore, the observed trends indicate that both P_I and P_{IV} have a minimal inhibitory effect on photopolymerization, reducing the reaction's intensity and overall efficiency. To effectively use poplar wood powders in photopolymerizable systems, it is essential to carefully optimize the formulation, production processes, and printing parameters to ensure a high degree of monomer conversion.

3.3 | 3D Printing of AESO-Based Samples by LCD

To ensure the best print quality and dimensional accuracy, the printing parameters were carefully optimized. The optimization

TABLE 4 | Printing parameters of AESO-based photocurable formulations.

Parameter	A-IB	A-IB + 3P_I	A-IB + 3P_{IV}
Layer height (mm)	0.100	0.100	0.100
Exposure time (s)	20	22	25
Bottom exposure time (s)	25	32	35
Rest time before lift (s)	1	1	1
Rest time after lift (s)	5	5	5
Rest time after retract (s)	3	3	3
Bottom lift distance (mm)	6	6	6
Lifting distance (mm)	6	6	6
Bottom retract distance (mm)	6	6	6
Retract distance (mm)	6	6	6
Bottom lift speed (mm min^{-1})	90	70	70
Lifting speed (mm min^{-1})	90	70	70
Bottom retract speed (mm min^{-1})	170	150	150
Retract speed (mm min^{-1})	170	150	150

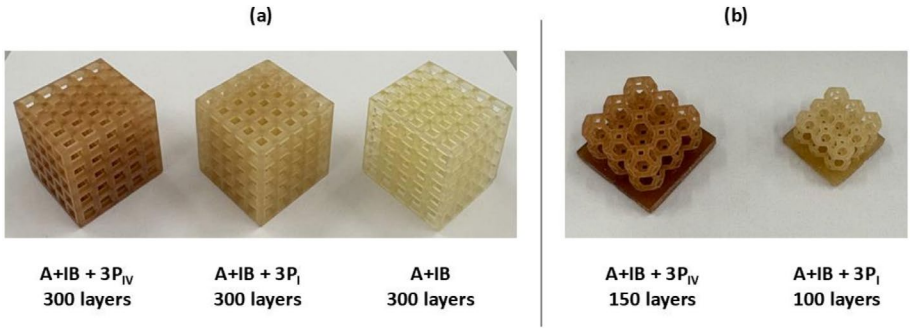

FIGURE 6 | High-density cubic lattice structures (a) and hierarchical 3D printed samples of (b).

TABLE 5 | Thermogravimetric properties and gel content of the AESO-based samples.

Sample code	Gel content (%)	$T_{5\%}$ [a] (°C)	$T_{maxdegr}$ [b] (°C)	Ash content[c] (%)
A-IB	99.7	260	317–401–558	0
A-IB + 3P$_I$	99.3	290	317–401–560	2
A-IB + 3P$_{IV}$	99.3	291	317–398-568	3

[a]$T_{5\%}$ represents the temperature at which 5% of the mass is lost.
[b]$T_{maxdegr}$ is the temperature at which the degradation rate is maximum.
[c]Ash content was evaluated at 900°C.

of exposure parameters was performed using the validation matrix provided by Phrozen. This approach allowed a systematic characterization of the printing conditions, aimed at defining the optimal values to ensure uniform polymerization, high detail resolution, and dimensional reproducibility consistent with the CAD model. The optimized printing parameters for the realization of the samples are summarized in Table 4.

Layer height was kept constant at 0.100 mm for all formulations to ensure good printing resolution. The irradiation times for the filled samples (A-IB + 3P$_I$ and A-IB + 3P$_{IV}$) were slightly increased from those used for A-IB; this elevation reflected the need to provide more energy to effectively photopolymerize in the presence of lignocellulosic particles. Bottom exposure time was also slightly increased with the addition of powders, thus ensuring good adhesion to the metal platform. Rest times and lift and retraction distances were kept equal for all formulations, to avoid mechanical distortions during vertical movement and to minimize interlayer defects. Meanwhile, the lifting and retraction speeds were set to be slower for the filled formulations, due to the increased viscosity. As previously mentioned, all photocured samples underwent posttreatment to complete the photopolymerization process.

After determining the appropriate printing parameters for each photocurable formulation, rectangular and dog bone-shaped specimens were realized via LCD for the characterization tests, and then different AESO-based photocured complex objects were successfully 3D printed, as shown in Figure 6.

Figure 6a presents high-density cubic lattices with fine spatial resolution, fabricated with the three tested formulations. Figure 6b shows two complex structures with a hierarchical design and internal voids. A visual inspection of the printed components reveals that the poplar-based composite samples exhibit high resolution and accuracy, strong layer adhesion, and well-defined edges, with minimal defects. Moreover, the complex structures maintain their geometry across all formulations, demonstrating that poplar-filled composites are capable of producing complex structures while maintaining structural integrity.

3.4 | Photocured Samples Characterizations

After printing the specimens for characterization tests, the morphological, thermal, viscoelastic, and mechanical properties of the AESO-based photocured samples and related composites were evaluated using different assays. The gel content represents the percentage by weight of the polymer network that remains insoluble in chloroform after undergoing extraction under defined conditions. All samples prepared were tested and showed satisfactory results, with gel content percentages exceeding 99% as reported in Table 5.

Table 5 provides a comparison of thermogravimetric data for all photocured samples, highlighting values related to thermal degradation and ash content. The results show a slight difference between the composites and poplar wood powders in the degradation starting temperature ($T_{5\%}$) and maximum degradation temperatures ($T_{degrmax}$).

Figure 7 presents the TGA (a) and DTG curves (b) of the printed poplar-filled samples.

The curves show that the presence of the powders does not substantially alter the thermal stability of the resin, as evidenced by the overlap of the first two peaks in the DTGs and the minimal variation in the last peak, which shows a slight increase (almost 10°C) only in the sample containing P$_{IV}$. The ash content is zero in the samples without filler, confirming the absence of inorganic components in the resin alone. Conversely, in the samples containing powders, an ash content of 2% was observed for A-IB + 3P$_I$ and 3% for A-IB + 3P$_{IV}$, likely due to the presence of inorganic materials in the powders that did not completely decompose during thermogravimetric analysis.

Figure 8 presents the SEM images acquired to examine the morphology of the unfilled and filled photocured specimens. Figure 8a,b shows the SEM micrographs of the fracture surface of the 3D printed A-IB sample without filler, at two different magnifications, which highlights a homogeneous and compact morphology, with well-adherent layers and no visible discontinuities or inclusions.

Figure 8c–f shows the SEM micrographs of the samples filled with poplar powders; both cases present a uniform distribution

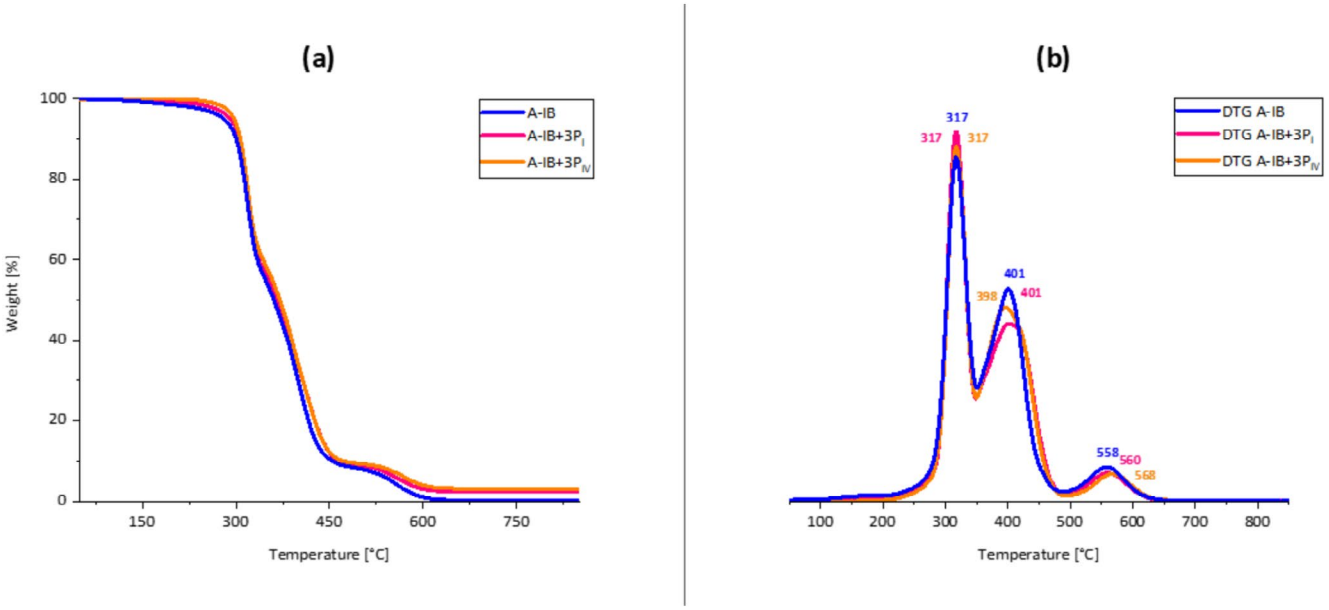

FIGURE 7 | TG (a) and DTG curves (b) of AESO-based samples.

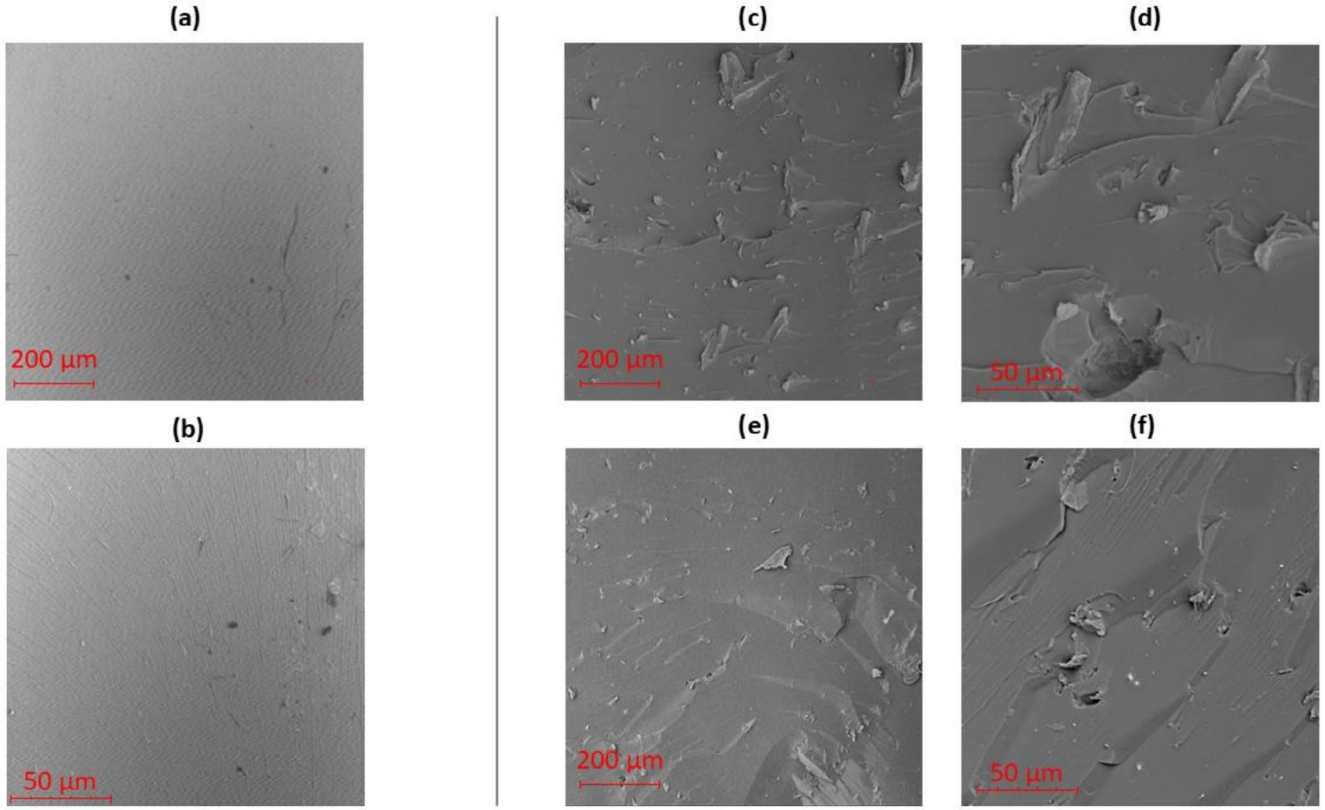

FIGURE 8 | SEM micrographs at different magnifications of AESO-based samples, 300× and 1500× of A-IB (a, b), A-IB + 3P$_I$ (c, d), and A-IB + 3P$_{IV}$ (e, f).

and good dispersion of the particles inside the AESO matrix. Furthermore, good adhesion between the fillers and the matrix is highlighted, since they are well integrated within the cross-linked polymer matrix.

Figure 9 presents a comparison of the DMTA curves for 3D printed samples. The A-IB sample exhibited a value of E' of 1.1 GPa. The incorporation of P_I and P_{IV} bio-fillers into the A-IB photocurable formulations significantly enhanced the storage modulus. This improvement is likely attributable to the stiffening effect induced on the filler particles, which restricts polymer chain mobility. In line with these findings, the inclusion of bio-fillers appears to increase the stiffness of the material in the glassy region, confirming their potential reinforcing role, although the differences are not substantial.

Table 6 summarizes the viscoelastic properties of the photocured samples, measured at 25°C. The storage modulus (E') indicates the elastic component of the material, while the loss modulus (E'') represents the viscous or dissipative component. Finally, the TanDelta value is the ratio between the E'' and the E'.

All formulations exhibit a similar reduction in E' as temperature increases, corresponding to the T_g, which is evident as a maximum of the peak of the TanDelta curves.

Furthermore, the TanDelta curves of A-IB + $3P_I$ and A-IB + $3P_{IV}$ show a broader profile compared to the unfilled A-IB sample, which reflects a wider distribution of segmental relaxation processes and implies increased structural heterogeneity, likely due to the presence of microdomains with variable polymer–filler interactions.

Thus, the addition of poplar wood powders not only modifies stiffness but also introduces more complex molecular dynamics within the polymer matrix.

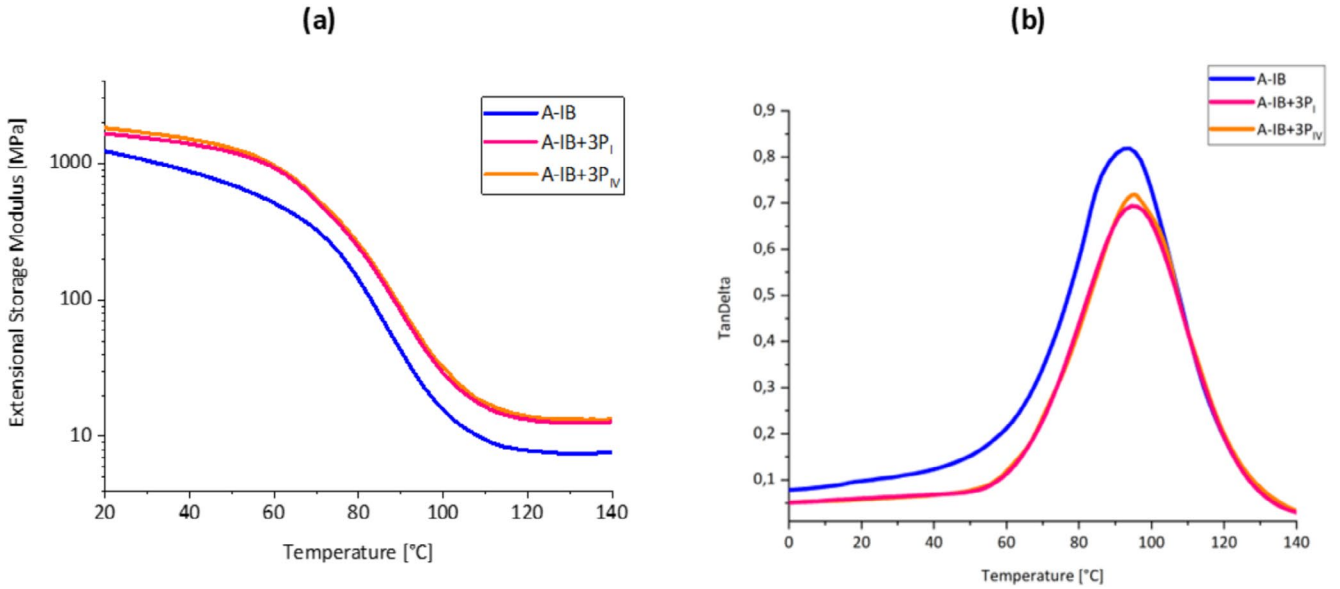

FIGURE 9 | DMTA curves of AESO-based samples, E' (a), and TanDelta (b).

TABLE 6 | Viscoelastic properties of AESO-based samples.

Sample code	E'@25°C (GPa)	E''@25°C (GPa)	$T_{TanDeltamax}$ (°C)	ν_e (mol m^{-3})
A-IB	1.1	0.1	92	9,5E+02
A-IB + $3P_I$	1.6	0.1	94	1,6E+03
A-IB + $3P_{IV}$	1.7	0.1	95	1,7E+03

TABLE 7 | Tensile properties of AESO-based samples.

Sample code	Young's modulus (MPa)	Ultimate tensile strength (MPa)	Elongation at break (%)
A-IB	634 ± 42	7 ± 1	29 ± 1
A-IB + $3P_I$	674 ± 16	33 ± 2	8 ± 1
A-IB + $3P_{IV}$	679 ± 11	31 ± 0	7.1 ± 0.1

From the comparison of the crosslink density values ν_e, also reported in Table 7, the addition of P_I and P_{IV} gives a significant increase in ν_e compared to that obtained for A-IB.

In conclusion, the incorporation of poplar powders within the thermoset matrix enhances crosslinking, improving the structural properties of the photocured polymer and promoting the formation of a denser, more robust 3D network. This behavior indicates good filler–matrix interaction and a positive effect of the poplar powders on the cross-linked structure.

Sample A-IB, considered as a reference, shows a Young's modulus of 634 MPa, an ultimate tensile strength (UTS) of 7 MPa, and an elongation at break of 29%. This indicates a material with good stiffness, fair mechanical strength, but poor deformation capacity.

With the addition of the P_I filler, the Young's modulus increases, a sign of greater stiffness of the material. While the elongation decreases dramatically by adding poplar powder, highlighting a much more ductile behavior.

Similar behavior is also observed in the sample filled with P_{IV}. The Young's modulus and UTS further increase, and the elongation at break decreases. Therefore, both P_I and P_{IV} increase the stiffness (Young's modulus) and the UTS of the material, but with a consequent reduction in deformability (elongation).

4 | Design of a Joint for Furniture

The furniture joints described in this paragraph represent one of the proofs of concept within the MICS program, which focuses on identifying, processing, and developing solutions to enhance the circularity of material resources in key Italian industrial sectors associated with the Made in Italy brand. The design and production of the joint represent the final stages of a research process that began with studying a specific production process, followed by a qualitative assessment of the potential for reusing the primary waste associated with it.

This effort culminated in experiments exploring the incorporation of such wastes into AM processes. The decision to focus on the design of joints for wood panels and components enables the project to seamlessly combine two of Italy's most iconic industries: wood products and furniture design. In research on designing furniture, particular attention is paid to the study of connecting elements between two-dimensional elements, such as panels, but also one-dimensional elements, such as laths [44, 45].

In the present paper, the bio-based composite formulations tested were used to produce via LCD 3DP joints for connecting two-dimensional panels and elements to be integrated into window frames. A survey of the main types of connections between flat panels was conducted as a preliminary step for designing the elements.

One of the most straightforward solutions for joining flat components is the Plywood connection. It utilizes plastic elements made from polyamide 6 and achieves secure fastening through a metal nut and bolt mechanism. This adjustable tightening system enables the connection of panels with varying thicknesses.

Additionally, the components are designed to accommodate multiple angle configurations, including 90°, 105°, and 150°. Other types of connections, like the joint designed by Ollè Gellèret [46], guarantee a secure hold through the friction generated with the panel. These joints are produced from nylon using two AM methods: one set via Fused Filament Fabrication (FFF) and the other through Selective Laser Sintering (SLS). The joint is designed to connect panels with an exact thickness of 8 mm and can accommodate angles of 45°, 90°, and 120°, depending on the available configurations.

Drawing inspiration from the connection systems developed by Plywood and designer Ollè, custom-sized joints suitable for 3DP were designed. The various configurations were modeled using the 3D software SketchUp, which was also used to generate the corresponding STL files. These files were then imported into CHITUBOX software to create print-ready files compatible with the 3D printer. The support structures were used during the printing process to ensure the best possible quality of the final object. Initial testing of the complex structures provided important feedback that guided refinements to the 3D model, enabling geometric modifications that improved both the functionality and overall efficiency of the project.

A series of objects was successfully printed as shown in Figure 10, including fasteners such as screws, nuts, bolts, and anchors with varying numbers of layers depending on the chosen model (a), components with relatively simple geometries, such as covers and square elements (b), and screw and fixed connections (c) and (d).

The corner plates, reported in Figure 10b, were designed and produced to act as connectors between panels in a window frame assembly. These components were installed in a wooden frame made entirely of poplar wood, where their primary function is to join the laths and panels, ensuring the structural stability of the entire frame. The connections were subsequently combined with 12 mm-thick plywood panels to explore various assembly configurations.

Figure 11 presents the first setup made, demonstrating how panels can be connected while remaining spaced apart, using both a screw-tight connection, as visible in Figure 11a,b, and a snap-fit connection, as illustrated in Figure 11c,d. The second configuration involves the use of plates and screws to create an interlocking connection between the two panels, as shown in Figure 11e,f.

5 | Conclusion

Incorporating poplar wood powders as bio-fillers into AESO-based photocurable resins enhances the mechanical and viscoelastic properties of the resulting materials. The thermal properties do not undergo major changes with the inclusion of powder dust in the A-IB systems.

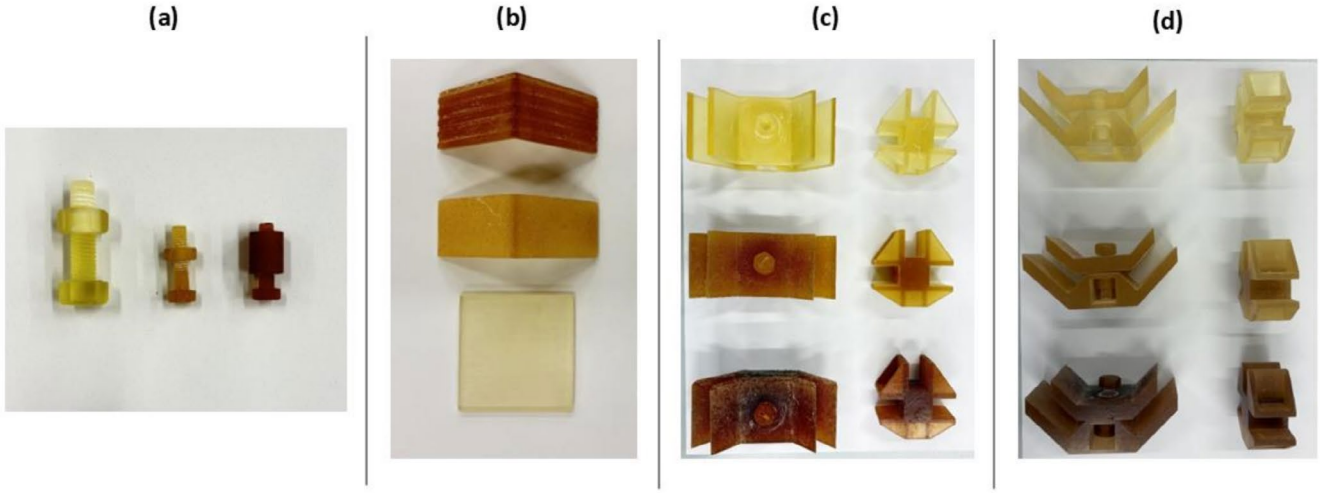

FIGURE 10 | Screws, nuts, bolts, and dowels (a), simple components such as covers and square elements (b), and screw and fixed connections (c, d).

The characterization of the powders through morphological analysis (SEM) shows that they do not show the presence of clusters or agglomerates that can lead to printing criticality. Thermal analysis shows that the major decomposition peaks are almost 300°C, which means that poplar powders show good thermal stability.

Rheological analyses on photocurable formulations demonstrate an increase in viscosity by adding the two poplar wood powders; however, the values remain within the optimal range for processing with M-SLA technology.

p-DSC analysis on liquid photosensitive formulations showed that the addition of poplar powders to the A-IB formulation reduces the intensity of the thermal peak (h_{peak}) and slightly slows down the reaction kinetics (t_{peak}), while maintaining the transition enthalpy (ΔH_{exp}) almost unchanged. These results indicate a slight inhibitory effect on photopolymerization by the P_I and P_{IV} powders, which led to the need to carefully optimize the formulation and the 3DP parameters to ensure high monomer conversions and resolutions of the final printed parts.

Additionally, the photo-cross–linked specimens were characterized by gel content, thermal, morphological, and mechanical properties, all of which provided insights into the structural integrity and performance of the composites. From a thermal perspective, adding poplar wood powders did not negatively impact the thermal stability. The characterization of the photocured material through SEM shows good adhesion between the bio-fillers and the cross-linked polymer matrix, with a uniform distribution of the powders.

The DMTA results show an increase in the E' and T_g values, indicating a stiffer structure. Furthermore, tensile tests reveal that the composites containing fillers exhibit a higher Young's modulus and greater UTS values, whereas the deformation capacity before breaking significantly decreases compared to the unmodified sample.

The collaboration between the Department of Applied Science and Technology and the Department of Architecture at the Politecnico di Torino has played a crucial role in achieving these results. On one hand, it has enabled the development and optimization of sustainable bio-based materials tailored for architectural and internal design uses. Moreover, these experimental materials have been successfully translated into real, functional components via AM, bridging the gap between scientific research and industrial design applications. This synergy has fostered innovation in both construction methods and prefabrication technologies: 3DP with bio-based composites opens new possibilities for low-impact construction systems.

Alternative assembly strategies, including modular connectors, window frames, and compact urban or household furnishings, were explored, demonstrating how the integration of advanced materials research with architectural experimentation can lead to more sustainable and creative solutions in the built environment.

Findings demonstrate that poplar wood powder waste can serve effectively as a bio-based filler in polymer composites, offering a sustainable and environmentally friendly alternative to traditional materials and supporting the advancement of greener manufacturing practices, with particular attention to the furniture sector.

Using AM processes increases the circularity of industrial production by enabling the reuse of waste and by-products in new or related supply chains. For instance, new synergies and business models could emerge between the wood panel and furniture production chains, fostering greater collaboration between the economic actors of the two sectors from an industrial symbiosis perspective. The use of bio-composites in construction and design fields can be expanded to include the production of additional cover plates and even frame sections for window frames. The results indicate that further development of components for the furniture sector using LCD-printed composites with poplar wood powders is possible. The specifics of 3DP technology have enabled the creation of objects with complex geometry, allowing the design and printing of connections for interior design applications. Due to the favorable mechanical properties of these composite materials,

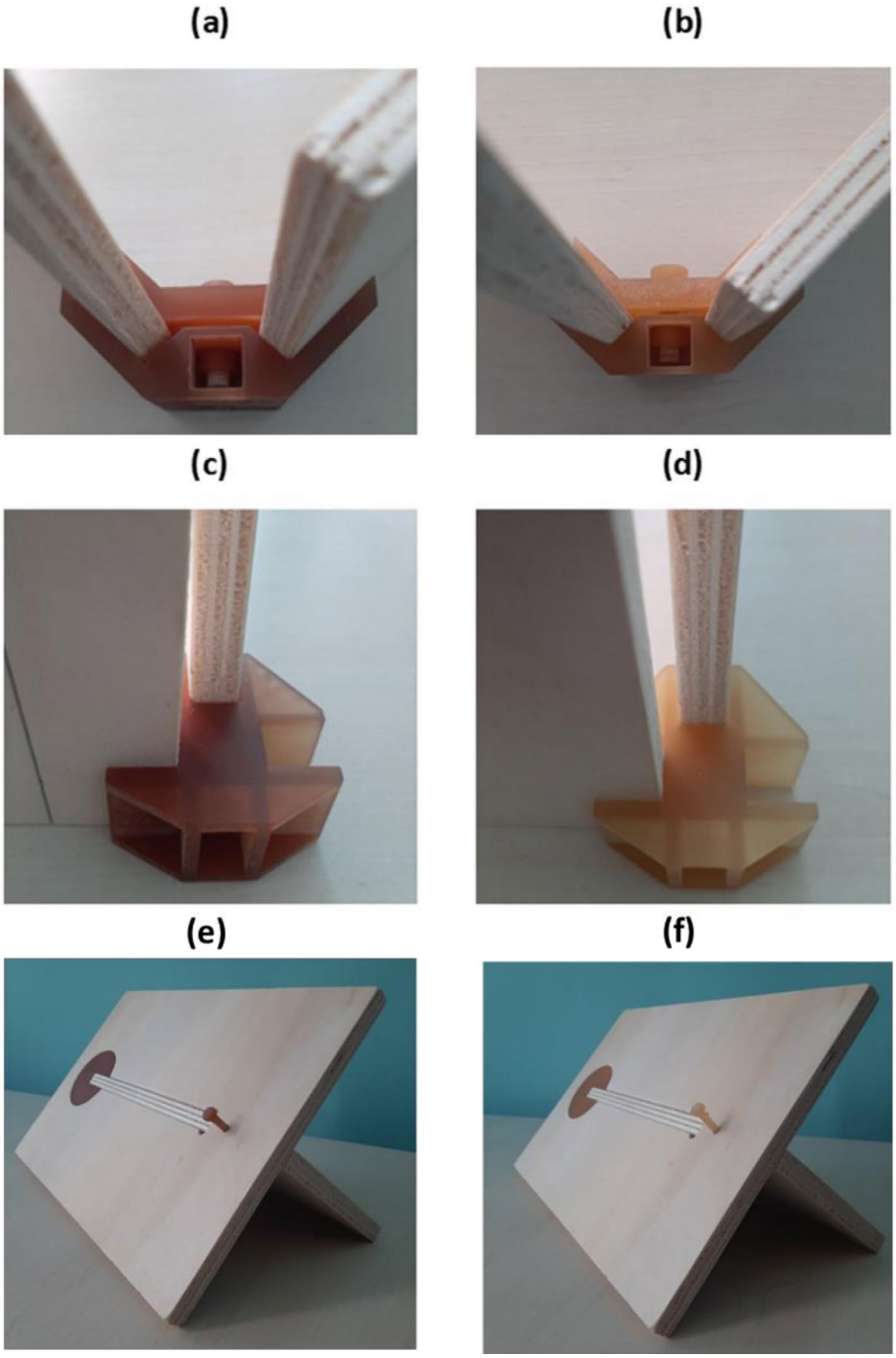

FIGURE 11 | Screw-tightening joint element based on A-IB + $3P_{IV}$ (a), A-IB + $3P_{I}$ (b), snap-fit connection element based on A-IB + $3P_{IV}$ (c), and A-IB + $3P_{I}$ (d). Plates between plywood panels based on A-IB + 3PIV (e) and A-IB + 3PI (f).

further studies can be conducted to develop connections between elements subjected to compressive and tensile forces greater than those presented in this article.

6 | Materials and Methods

6.1 | Materials

AESO, a bio-based photopolymerizable resin, was chosen as a bio-based starting photocurable resin for the formulation. It has a density of 1.04 g mL^{-1} and a viscosity ranging from 15 to 38 Pa s at 25°C. However, to meet the requirements of VPP technology, which requires viscosities lower than 1 Pa s [41]. It was necessary to add a reactive diluent; for this purpose, isobornyl methacrylate (IBOMA), a bio-based monomer derived from pine, was used. This compound, with a density of 0.983 g mL^{-1} at 25°C, has low viscosity and reduced shrinkage potential. It actively participates in polymerization, becoming part of the final polymer network, as well as reducing the viscosity of the mixture, improving its printability both in pure and in loaded with poplar wood powders forms [47]. Phenyl bis (2,4,6-trimethylbenzoyl) phosphine oxide (BAPO) was chosen as a radical photoinitiator. BAPO is a type I radical

FIGURE 12 | Raw poplar wood P_I (a) and briquettes P_{IV} (b).

TABLE 8 | Material names and related codes.

Material name	Code
Acrylate epoxidized soybean oil (AESO)	A
Isobornyl methacrylate (IBOMA)	IB
Poplar wood powder type I	P_I
Poplar wood powder type IV	P_{IV}

photoinitiator that undergoes a homolytic bond cleavage upon irradiation to yield free radicals. BAPO offers several advantages, including a short triplet lifetime resulting in high photoactivity and blue-shifted absorption, making it suitable for use in visible light. It also undergoes photobleaching, a process in which it loses optical absorbance during radical formation, resulting in the formation of uncolored photoproducts, enabling the production of colorless photocured samples [48].

AESO, IBOMA, and BAPO for the preparation of photocurable formulations were purchased from Merck (Darmstadt, Germany). Two different bio-filler powders, poplar wood powders type I (PI) and type IV (PIV), were incorporated within the AESO-based photocurable formulations to prepare the final composites, each added at 3 phr (per hundred parts of resin).

6.2 | Poplar Powders Preparation

The feedstocks used to produce the P_I and P_{IV} poplar powders were roundwood and wood dust, respectively, as shown in Figure 12.

P_I was prepared by milling flakes and fragments of raw poplar round wood in an electric powder machine (blade mill) for 20 min. The resulting powder was sieved manually using a sieve with a mesh size of less than 100 μm for about 30 min. Whereas P_{IV} was prepared by grinding plywood production waste as briquettes in an electric powder machine (blade mill) for 2 min. The resulting powder was then sieved manually using a sieve with a mesh size of less than 100 μm for approximately 45 min. The corresponding acronyms for reagents and the two poplar powders used in this research project are listed in Table 8.

6.3 | Preparation of Photocurable Formulations

Photocurable formulations were prepared by mixing AESO and IBOMA in a 50:50 weight ratio. This ratio was selected after several rheological tests varying the AESO and IBOMA content from 100 to 0 wt%, as it resulted in a viscosity close to the optimal value required for VPP [41], thus ensuring good printability [13].

Formulations were prepared by mixing AESO and IBOMA with magnetic stirring for 3 h at 25°C. Then, Ultra-Turrax T10 Basic S1 (UT) was used at around 25,000 rpm for 5 min, followed by 10 min of ultrasonic bath (UB) at room temperature. Then, 3 phr of bio-fillers were added to the formulation by using UT for 5 min at 25000 rpm. Subsequently, the 10-min step of UB at room temperature was repeated. Finally, 2 phr of BAPO was added within the formulation by mixing it for 5 min with UT at 25,000 rpm, and 10 min in an UB at 60°C, with a degassing tool, was performed.

A series of sedimentation tests was first performed to assess whether the formulation components tend to separate over time and settle at the container bottom. Monitoring sediment formation is crucial for the 3DP process, as material deposition can lead to printing errors and result in components with variable mechanical behavior. Each formulation incorporating powders underwent sedimentation evaluation, with observations recorded continuously over a 1 to 24-h period. These findings also contributed to identifying the most suitable geometry for printed parts, which depends significantly on both print duration and filler concentration. The stability of the A-IB formulations filled with 3 phr of powder over time is shown sequentially in Figure 13. At time zero, both P_I and P_{IV} dispersions appeared homogeneous, as illustrated in Figure 13a.

After 8 h, the formulations remained stable and printable, with no significant sedimentation observed, as shown in Figure 13b. However, by the 24-h mark, sedimentation occurred in both samples, with P_{IV} settling more evidently than P_I, as depicted in Figure 13c.

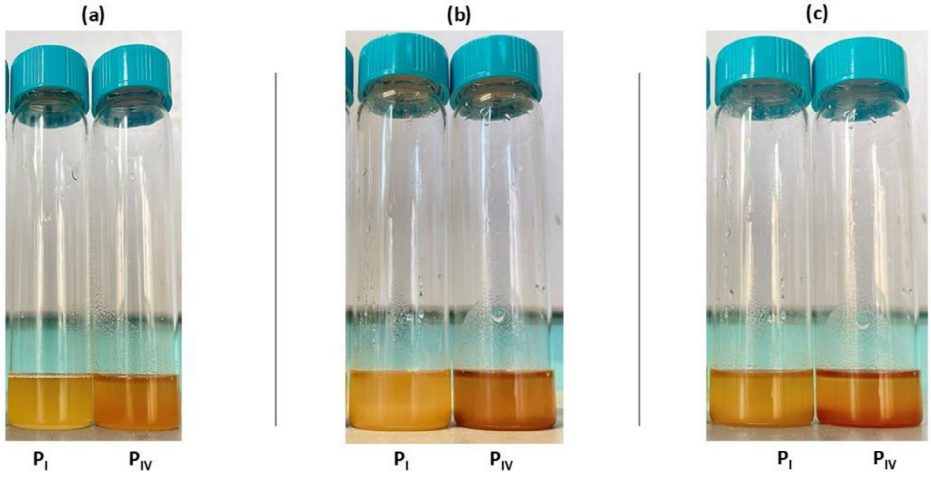

FIGURE 13 | Sedimentation tests for A-IB formulations filled with 3 phr of poplar wood powders, after 0 h (a), 8 h (b), and 24 h (c), respectively.

6.4 | 3D Printing Process

Photocurable formulations were 3D printed with a Phrozen Sonic Mini 8K VPP (Phrozen, Hsinchu City, Taiwan), a printer that operates using LCD technology in a bottom-up configuration that reduces the amount of resin in the vat at any one time, saving materials and costs [11]. This includes slicer software called CHITUBOX V1.9.0, which enables loading the STL file of the desired part, selecting its orientation, and applying supports to connect the piece to the printing platform. The software also allows adjustments of printing parameters such as layer thickness, exposure time, and speed during the printing process. The photocured samples were detached from the build platform, washed with 2-isopropanol alcohol (Merck—Darmstadt, Germany) for 15 min, then air-dried for 24 h, and subsequently post-cured at 25°C for 60 min using an Anycubic Wash & Cure Plus machine (Anycubic Technology Co., Hong Kong) equipped with a UV lamp of 405 nm.

Acknowledgments

The authors would like to thank professors Roberto Zanuttini and Francesco Negro of the Department of Agricultural, Forest and Food Sciences (University of Turin), Toro Compensati Srl, Panguaneta Spa, and Opendot Foundation for testing the 3D components. This research is the result of the collaboration between two research groups of the Politecnico di Torino working within the research partnership, "Made in Italy Circolare e Sostenibile (MICS)". These groups belong to two specific projects called "Circular design for natural fibers" related to spoke 2 "Eco-Design strategies: from materials to Product Service Systems—PSS" and "Innovative polymers and polymer-based composites for engineering and design applications" related to spoke 6 "Additive Manufacturing as disruptive enabler of the Twin Transition." The objective of the research partnership is to foster competitive research between universities and industry to explore innovative practices toward sustainability and circularity of the main Made in Italy production chains. Open access publishing facilitated by Politecnico di Torino, as part of the Wiley - CRUI-CARE agreement.

Funding

The present work was supported by the European Union Next-Generation EU (PIANO NAZIONALE DI RIPRESA E RESILIENZA (PNRR)—MISSIONE 4 COMPONENTE 2, INVESTIMENTO 1.3—D.D. 1551.11-10-2022, PE00000004). The paper reports only the authors' viewpoints, neither the European Union nor the European Commission are responsible for them.

Conflicts of Interest

The authors declare no conflicts of interest.

References

1. A. Alammar, J. C. Kois, M. Revilla-León, and W. Att, "Additive Manufacturing Technologies: Current Status and Future Perspectives," *Journal of Prosthodontics* 31 (2022): 4–12.

2. F. Calignano, D. Manfredi, E. P. Ambrosio, et al., "Overview on Additive Manufacturing Technologies," *Proceedings of the IEEE* 105 (2017): 593–612.

3. L. J. Tan, W. Zhu, and K. Zhou, "Recent Progress on Polymer Materials for Additive Manufacturing," *Advanced Functional Materials* 30 (2020): 1.

4. ISO/ASTM 52900:2015, "Additive Manufacturing—General Principles—Terminology (ISO/ASTM 52900:2015)," 2017.

5. M. Shah, A. Ullah, K. Azher, et al., "Vat Photopolymerization-Based 3D Printing of Polymer Nanocomposites: Current Trends and Applications," *RSC Advances* 13 (2023): 1456–1496.

6. H. A. Colorado, E. I. G. Velásquez, and S. N. Monteiro, "Sustainability of Additive Manufacturing: The Circular Economy of Materials and Environmental Perspectives," *Journal of Materials Research and Technology* 9 (2020): 8221–8234.

7. A. Jandyal, I. Chaturvedi, I. Wazir, A. Raina, and M. I. Ul Haq, "3D Printing – A Review of Processes, Materials and Applications in Industry 4.0," *Sustainable Operations and Computers* 3 (2022): 33–42.

8. S. C. Ligon, R. Liska, J. Stampfl, M. Gurr, and R. Mülhaupt, "Polymers for 3D Printing and Customized Additive Manufacturing," *Chemical Reviews* 117 (2017): 10212–10290.

9. N. Guo and M. C. Leu, "Additive Manufacturing: Technology, Applications and Research Needs," *Frontiers of Mechanical Engineering* 8 (2013): 215–243.

10. P. Lakkala, S. R. Munnangi, S. Bandari, and M. Repka, "Additive Manufacturing Technologies With Emphasis on Stereolithography 3D Printing in Pharmaceutical and Medical Applications: A Review," *International Journal of Pharmaceutics: X* 5 (2023): 5, https://doi.org/10.1016/j.ijpx.2023.100159.

11. F. Sacchi, G. Colucci, F. Bondioli, M. Sangermano, and M. Messori, "Review: Bio-Based Photopolymers for Additive Manufacturing," *Journal of Materials Science* 60 (2025): 11191–11220.

12. C. Tosto, E. Pergolizzi, I. Blanco, et al., "Epoxy Based Blends for Additive Manufacturing by Liquid Crystal Display (LCD) Printing: The Effect of Blending and Dual Curing on Daylight Curable Resins," *Polymers (Basel)* 12 (2020): 1594, https://doi.org/10.3390/polym12071594.

13. G. Colucci, F. Sacchi, F. Bondioli, and M. Messori, "Fully Bio-Based Polymer Composites: Preparation, Characterization, and LCD 3D Printing," *Polymers (Basel)* 16 (2024): 1272–1287, https://doi.org/10.3390/polym16091272.

14. A. Al Rashid, S. A. Khan, S. G. Al-Ghamdi, and M. Koç, "Additive Manufacturing: Technology, Applications, Markets, and Opportunities for the Built Environment," *Automation in Construction* 118 (2020): 103268, https://doi.org/10.1016/j.autcon.2020.103268.

15. F. Habib and M. Bajpai, "Synthesis and Characterization of Acrylated Epoxidized Soybean Oil for UV-Cured Coatings," *Chemistry & Chemical Technology* 5 (2011): 317–326, https://doi.org/10.23939/chcht05.03.317.

16. S. Batarseh, N. Goldsberry, C. Handysides, et al., "Comparison of Volumetric Change in Objects Printed With LCD and DLP 3D Printers," *Journal of the California Dental Association* 51 (2023): 2271641, https://doi.org/10.1080/19424396.2023.2271641.

17. S. Chen, Q. Zhang, Z. Yang, et al., "Fabrication and Characterization of Light-Curing Soybean Oil-Based Epoxy Resin Applied for LCD Additive Manufacturing," *Industrial Crops and Products* 202 (2023): 117037, https://doi.org/10.1016/j.indcrop.2023.117037.

18. E. Skliutas, M. Lebedevaite, S. Kasetaite, et al., "A Bio-Based Resin for a Multi-Scale Optical 3D Printing," *Scientific Reports* 10 (2020): 10, https://doi.org/10.1038/s41598-020-66618-1.

19. M. Calovi and S. Rossi, "Functional Olive Pit Powders: The Role of the Bio-Based Filler in Reducing the Water Uptake Phenomena of the Waterborne Paint," *Coatings* 13 (2023): 442, https://doi.org/10.3390/coatings13020442.

20. G. Colucci, F. Sacchi, F. Bondioli, and M. Messori, "3D Printing of Lignin-Based Polymeric Composites Obtained Using Liquid Crystal Display as a Vat Photopolymerization Technique," *Polymer International* 74 (2025): 828–838, https://doi.org/10.1002/pi.6783.

21. G. Colucci, F. Sacchi, M. Checchi, et al., "Development and 3D Printing of AESO-Based Composites Containing Olive Pit Powder," *Journal of Composites Science* 9 (2025): 479.

22. G. Colucci, F. Di Stefano, F. Sacchi, et al., "Bio-Based Polymer Composites Obtained by Vat Photopolymerization of Photocurable Resins Modified With Biochar as Sustainable Filler," *Composites Part A, Applied Science and Manufacturing* 198 (2025): 109102, https://doi.org/10.1016/j.compositesa.2025.109102.

23. M. Lebedevaite, A. Gineika, V. Talacka, K. Baltakys, and J. Ostrauskaite, "Development and Optical 3D Printing of Acrylated Epoxidized Soybean Oil-Based Composites With Functionalized Calcium Silicate Hydrate Filler Derived From Aluminium Fluoride Production Waste," *Composites Part A, Applied Science and Manufacturing* 157 (2022): 106929, https://doi.org/10.1016/j.compositesa.2022.106929.

24. J. Narewska, L. Lassila, and P. Fardim, "Preparation and Characterization of New Mouldable Cellulose-AESO Biocomposites," *Cellulose* 21 (2014): 1769–1780.

25. A. Navaruckiene, E. Skliutas, S. Kasetaite, et al., "Vanillin Acrylate-Based Resins for Optical 3D Printing," *Polymers (Basel)* 12 (2020): 397, https://doi.org/10.3390/polym12020397.

26. C. Noè, A. Cosola, C. Tonda-Turo, et al., "DLP-Printable Fully Biobased Soybean Oil Composites," *Polymer (Guildf)* 247 (2022): 124779, https://doi.org/10.1016/j.polymer.2022.124779.

27. E. Sanchez-Rexach, T. G. Johnston, C. Jehanno, H. Sardon, and A. Nelson, "Sustainable Materials and Chemical Processes for Additive Manufacturing," *Chemistry of Materials* 32 (2020): 7105–7119.

28. J. F. Stanzione, P. A. Giangiulio, J. M. Sadler, J. J. La Scala, and R. P. Wool, "Lignin-Based Bio-Oil Mimic as Biobased Resin for Composite Applications," *ACS Sustainable Chemistry & Engineering* 1 (2013): 419–426.

29. V. S. D. Voet, J. Guit, and K. Loos, "Sustainable Photopolymers in 3D Printing: A Review on Biobased, Biodegradable, and Recyclable Alternatives," *Macromolecular Rapid Communications* 42 (2021): 2000475, https://doi.org/10.1002/marc.202000475.

30. D. J. Gardner and L. Wang, "Additive Manufacturing of Wood-Based Materials for Composite Applications," 2019.

31. J. J. Balatinecz and D. E. Kretschmann, *Poplar Culture in North America, Part A* (National Research Council Of Canada, 2001), 277–291.

32. P. Sannigrahi, A. J. Ragauskas, and G. A. Tuskan, "Poplar as a Feedstock for Biofuels: A Review of Compositional Characteristics," *Biofuels, Bioproducts and Biorefining* 4 (2010): 209–226.

33. G. Castro, R. Zanuttini, and G. Fragnelli, *La Pioppicoltura e Il Compensato Di Pioppo Dell'industria Italiana* (Lampi Di Stampa Collana Federlegno, 2014).

34. A. Regattieri and G. Bellomi, "Innovative Lay-Up System in Plywood Manufacturing Process," *European Journal of Wood and Wood Products* 67 (2009): 55–62.

35. G. Vacchiano, P. M. Chiarabaglio, M. Faccoli, and G. Minotta, "Il Contributo Della Ricerca Italiana All'intensificazione Sostenibile in Agricoltura," in *Proceedings of the 18th AISSA Conference, I Quaderni di AISSA*, vol. 3 (2022), 11–21.

36. V. K. Lyubov and A. N. Popov, "Plywood Production Wastes to Energy," *Journal of Physics Conference Series* 891 (2017): 012219, https://doi.org/10.1088/1742-6596/891/1/012219.

37. L. Pezzana, G. Melilli, P. Delliere, et al., "Thiol-Ene Biobased Networks: Furan Allyl Derivatives for Green Coating Applications," *Progress in Organic Coatings* 173 (2022): 107203, https://doi.org/10.1016/j.porgcoat.2022.107203.

38. G. Colucci, A. Aluigi, C. Tonin, and R. Bongiovanni, "Photopolymerization of Keratin-Based Thiol-Ene Coatings," *Progress in Organic Coating* 77 (2014): 1104–1110.

39. T. Hatakeyama, S. Yamashita, and H. Hatakeyama, "Thermal Properties of Lignin-Based Polycaprolactones," *Journal of Thermal Analysis and Calorimetry* 143 (2021): 203–211.

40. S. Elkhalifa, P. Parthasarathy, H. R. Mackey, et al., "Synthesis of Activated Carbon From Lemna Minor Plant and Magnetized With Iron (III) Oxide Magnetic Nanoparticles and Its Application in Removal of Ciprofloxacin," *Biomass Conversion and Biorefinery* 12 (2022): 1.

41. M. Lebedevaite, V. Talacka, and J. Ostrauskaite, "High Biorenewable Content Acrylate Photocurable Resins for DLP 3D Printing," *Journal of Applied Polymer Science* 138 (2021): 50233, https://doi.org/10.1002/app.50233.

42. D. N. Lastovickova, F. R. Toulan, J. R. Mitchell, et al., "Resin, Cure, and Polymer Properties of Photopolymerizable Resins Containing Bio-Derived Isosorbide," *Journal of Applied Polymer Science* 138 (2021): 50574, https://doi.org/10.1002/app.50574.

43. S. A. Wajihah and D. S. Sankar, "A Review on Non-Newtonian Fluid Models for Multi-Layered Blood Rheology in Constricted Arteries," *Archive of Applied Mechanics* 93 (2023): 1771–1796.

44. B. Petrova and V. Jivkov, "Application of 3D Printing Technology in Furniture Construction," *Materials* 17 (2024): 4848, https://doi.org/10.3390/ma17194848.

45. A. Nicolau, M. A. Pop, S. V. Georgescu, and C. Coșereanu, "Application of Additive Manufacturing Technology for Chair Parts Connections," *Applied Sciences* 13 (2023): 12044, https://doi.org/10.3390/app132112044.

46. C. C. Chen, W. Z. Yang, H. M. Teng, S. S. Liao, and C. C. Tsao, "Study on the Application of 3D Printing to Wooden Furniture Connectors," *Journal of Physics Conference Series* 2631 (2023): 012006, https://doi.org/10.1088/1742-6596/2631/1/012006.

47. A. R. M. Martins, I. D. Silva, L. Machado-Santos, R. P. Vitti, M. A. C. Sinhoreti, and W. C. Brandt, "Isobornyl Methacrylate as Diluent Co-Monomer on Physical-Mechanical Properties of Dental Resin Composites," *Journal of Applied Polymer Science* 138 (2021): 50498, https://doi.org/10.1002/app.50498.

48. F. Dumur, "Recent Advances on Photobleachable Visible Light Photoinitiators of Polymerization," *European Polymer Journal* 186 (2023): 111874, https://doi.org/10.1016/j.eurpolymj.2023.111874.